

Time-domain Travelling-wave Model for Quantum Dot Passive Mode-locked Lasers

Original

Time-domain Travelling-wave Model for Quantum Dot Passive Mode-locked Lasers / Rossetti, Mattia; Bardella, Paolo; Montrosset, Ivo. - In: IEEE JOURNAL OF QUANTUM ELECTRONICS. - ISSN 0018-9197. - STAMPA. - 47:2(2011), pp. 139-150. [10.1109/JQE.2010.2055550]

Availability:

This version is available at: 11583/2374778 since:

Publisher:

IEEE-INST ELECTRICAL ELECTRONICS ENGINEERS INC, 445 HOES LANE, PISCATAWAY, NJ 08855-4141 USA

Published

DOI:10.1109/JQE.2010.2055550

Terms of use:

This article is made available under terms and conditions as specified in the corresponding bibliographic description in the repository

Publisher copyright

(Article begins on next page)

Time-Domain Travelling-Wave Model for Quantum Dot Passively Mode-Locked Lasers

Mattia Rossetti, Paolo Bardella, and Ivo Montrosset, *Member, IEEE*

Abstract—We present a time-domain travelling-wave model for the simulation of passive mode-locking in quantum dot (QD) lasers; accurate expressions for the time varying QD optical susceptibility and the QD spontaneous emission noise source are introduced in the 1-D wave equations and numerically described using a set of infinite-impulse response filters. The inhomogeneous broadening of the density of states of the whole QD ensemble as well as the homogeneous linewidth of each QD interband transition are properly taken into account in the model. Population dynamics in the QD, quantum well, and barrier states under both forward and reverse bias conditions are modeled via proper sets of multi-population rate equations coupled with the field propagation equations. The model is first applied to the study of gain and absorption recovery in a QD semiconductor optical amplifier under both forward and reverse bias conditions. Simulations of passive mode-locking in a two-section QD laser are then performed as a function of the bias parameters. Gain and absorption dynamics leading to the generation of mode-locking pulses is described. The onset of a trailing-edge instability at low currents is observed and fully explained in the framework of the described model.

Index Terms—Mode-locked lasers, modeling, quantum dots, semiconductor optical amplifiers.

I. INTRODUCTION

PASSIVELY mode-locked (ML) lasers based on self-assembled semiconductor quantum dots (QD) have shown superior properties compared to their bulk and quantum-well (QW) counterparts due to the peculiar properties of the QD active medium: thanks to the inhomogeneous gain broadening induced by the QD size dispersion, a broad gain bandwidth can be achieved [1]. Also, QD-based devices show large gain saturation energies and large differential absorption due to the small density of states of the whole QD ensemble. Moreover, ultrafast gain recovery induced by efficient carrier capture and relaxation in the QD states as well as fast absorption recovery obtained in reverse-biased QD structures have been measured via differential transmission spectroscopy (DTS) experiments [2], [3].

Such properties significantly contribute to the efficient generation of picosecond and subpicosecond pulses at elevated bit rates in two-section passively ML lasers with the active

region consisting of several layers of InAs QDs emitting around $1.3 \mu\text{m}$ [4]–[7]. These devices show small sensitivity to Q-switching instability [8], low chirp, as well as low amplitude noise and low timing jitter [9].

In past years, different approaches have been used to model the ML regimes in QD lasers: models based on delayed differential equations [10] have been proved to be a powerful method to study the stability and evolution of the ML regimes as a function of the applied bias conditions [8]. In [11], a frequency domain approach has been applied to study active ML in a QD laser, considering a detailed description of the optical response of the inhomogeneously broadened QD active medium.

In this paper, we present an alternative approach to the analysis of passive ML in QD lasers based on a time-domain travelling-wave model [12]. Within this approach, the propagation equations describing the spatiotemporal field dynamics in the laser cavity are directly solved numerically, using a finite-difference scheme. Compared to the models described in [10] and [11], no assumption on the geometry of the laser cavity or on the strength of gain/absorption modulation governing the ML regimes are required. Moreover, with respect to existing time-domain travelling-wave models [12], a detailed description of the QD optical susceptibility, spontaneous emission noise, and population dynamics in the QD states is fully included in the model, allowing a complete study of the peculiar QD optical properties governing the dynamics of multisection QD ML lasers.

The paper is organized as follows. In Section II, the implemented numerical model is presented. In Section III, simulations of DTS experiments in forward- and reverse-biased semiconductor optical amplifiers (SOAs) are shown; these results allowed gaining insights into the peculiar properties of QD gain and absorption dynamics. Moreover, comparison with published experimental results allowed validation of the chosen model parameters. In Section IV, passive mode-locking in a two-section QD laser is then investigated as a function of both reverse voltage and gain current. The regime of stable ML is outlined, gain and absorption dynamics governing the generation of the ML pulses is studied, and the onset of a trailing edge instability at low currents is observed and explained. Finally, in Section V a brief conclusion is drawn.

II. NUMERICAL MODEL

The longitudinal propagation of the transverse-electric guided mode in the laser cavity can be described by the

second-order differential equation as follows:

$$\begin{aligned} \frac{\partial^2 E(z, t)}{\partial z^2} - \frac{1}{c^2} \frac{\partial^2}{\partial t^2} (\eta^2 E(z, t)) \\ = \mu_0 \frac{\partial^2 P(z, t)}{\partial t^2} + \mu_0 \frac{\partial J_S(z, t)}{\partial t} \end{aligned} \quad (1)$$

where $E(z, t)$ is the mode amplitude, η is the background effective refractive index of the guided mode, μ_0 is the vacuum magnetic permeability, $P(z, t)$ is the electric polarization induced by the QD active medium, and $J(z, t)$ is an effective current density accounting for the spontaneous emission noise source from the QDs.

In the following paragraphs, suitable expressions for the QD polarization and spontaneous emission noise are defined and equations for the interband and intraband dynamics of carrier populations in the QDs are described. Finally, the approximations introduced in (1) and the numerical solution via a finite-difference approach are outlined.

A. QD Optical Susceptibility and Spontaneous Emission Rate

Throughout this paper, multilayered structures composed by InAs QD layers embedded in InGaAs/GaAs QWs (dot-in-a-well) and emitting at around $1.3 \mu\text{m}$ will be considered. A schematic of the related energy diagram is shown in Fig. 1(a) and (b). Confined states for carriers in the QDs are supposed to consist of a two-fold degenerate ground state (GS) and two excited states (ES₁ and ES₂), with degeneracy equal to 4 and 6, respectively. At higher energies, a continuum of states belonging to the QW and 3-D states in the GaAs separate-confinement heterostructure (SCH) are considered.

Due to the self-assembling growth process, a dispersion in the QD sizes occurs, inducing an inhomogeneous broadening of the density of states of the whole QD system [1]. In order to account for this property, in the model the whole QD ensemble is subdivided in N populations; QDs belonging to the same population are assumed to be identical, having therefore the same characteristic interband transition energies $\hbar\bar{\omega}_{im}$ and carrier occupation probabilities in the confined states ρ_{im} , where index $i = 1, \dots, N$ (N odd) refers to the i th QD population whereas index $m = \text{GS}, \text{ES}_1, \text{ES}_2$ refers to the m th QD confined state. The QD size dispersion and therefore the inhomogeneous broadening of the QD density of states are assumed to follow a Gaussian distribution function. The existence probability of the i th QD population will be therefore [11]

$$G_i = \frac{1}{Z} \exp\left(-4 \ln 2 \times \frac{(\hbar\bar{\omega}_{i,GS} - \hbar\bar{\omega}_{(N+1)/2,GS})^2}{\Delta E^2}\right) \quad (2)$$

where ΔE is the Gaussian full-width at half-maximum (FWHM) and Z is a constant such that $\sum_i G_i = 1$.

The QD polarization $P(z, t)$ can be expressed via the optical susceptibility of the QD active medium as follows:

$$P(z, t) = \varepsilon_0 \int_{-\infty}^t \chi(\{\rho_{im}\}, t - \tau) E(z, \tau) d\tau \quad (3)$$

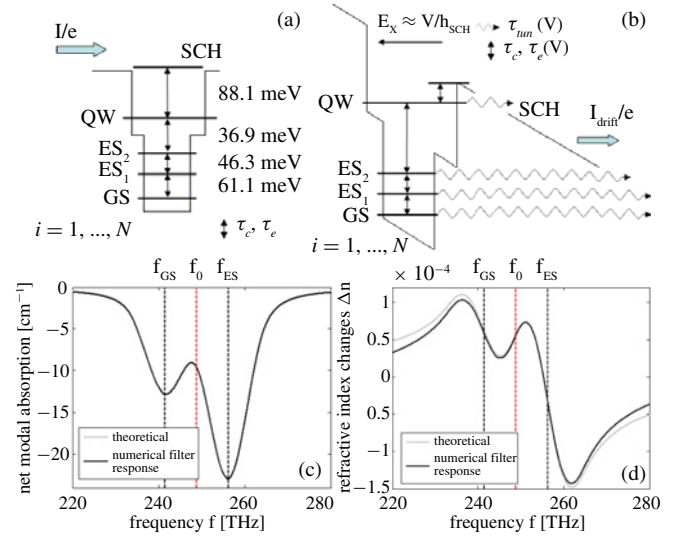


Fig. 1. (a) Schematic of the energy diagram of the dot-in-a-well layers under forward bias condition; numerical values indicate energy differences between confined states for the QD group with highest existence probability. (b) Schematic of the energy diagram in a reverse bias condition, symbol \rightsquigarrow denotes tunneling processes. (c–d) Comparison between the theoretical QD absorption and related refractive index spectra at zero bias (black) and the response of the numerical filters for a time step $\Delta t = 10$ fs (gray); dashed lines indicate the reference frequency for the slowly varying envelope approximation (f_0) and GS (f_{GS}) and ES (f_{ES}) absorption peaks, respectively.

where ε_0 is the vacuum electric permittivity. The QD susceptibility $\chi(\{\rho_{im}\}, t)$ depends on the carrier occupation probabilities $\{\rho_{im}\}$ of the confined states in the whole ensemble of QDs and, as already pointed out, it is inhomogeneously broadened due to the QD size dispersion.

With these assumptions, the Fourier transform of the QD susceptibility appearing in (3) can be written as the superposition of single Lorentzian contributions representing the homogeneous line broadening of the interband transitions from the QD GS and ES₁ of each QD population [1], [11] as follows:

$$\begin{aligned} \chi(\{\rho_{im}\}, \omega) &= F\left\{\chi(\{\rho_{im}\}, t)\right\} = \sum_{i=1}^N \sum_{\substack{m= \\ \text{GS}, \text{ES}_1}} \chi_{im}(\rho_{im}, \omega) \\ &= \frac{\Gamma_{xy}}{h_W} N_D \sum_{i=1}^N \sum_{\substack{m= \\ \text{GS}, \text{ES}_1}} G_i D_m A_m \frac{j}{\hbar \pi} \frac{1}{\Gamma + j(\omega - \bar{\omega}_{im})} (2\rho_{im} - 1) \end{aligned} \quad (4)$$

where $1/\Gamma$ represents the characteristic dephasing time of the interband transition, A_m is a coefficient containing the interband transition matrix element for the m th transition ($m = \text{GS}, \text{ES}_1$), D_m is the degeneracy of the m th QD state, N_D is the QD surface density, Γ_{xy} is the field confinement factor in the QD layers, and h_W is the QW width.

Contributions from the upper QD excited (ES₂), WL, and SCH states to the optical susceptibility (4) have been neglected, being considerably detuned with respect to the lasing frequencies. On the contrary, contributions from the first ES of each QD group have been properly described since refractive index changes induced by the ES population dynamics are expected to be the main cause for a nonzero frequency chirp of the ML pulses [13].

One must point out that the carrier distribution in the QD states depends on time: $\rho_{im} = \rho_{im}(z, t)$. However, it is reasonable to assume that population dynamics in the QDs is much slower than the characteristic dephasing time $1/\Gamma$, $|\rho_{im}^{-1} \partial \rho_{im} / \partial t| \ll \Gamma$. In such a case, the temporal changes in the optical polarization induced by the population dynamics in the QD states can be treated within an adiabatic approximation. Time-dependent gain and refractive index spectra induced by the QDs are therefore defined as $g(z, t, \omega) = (\omega/c\eta) \text{Im} \chi(\{\rho_{im}(z, t)\}, \omega)$ and $\Delta\eta(z, t, \omega) = (1/2\eta) \text{Re} \chi(\{\rho_{im}(z, t)\}, \omega)$, respectively.

The density of spontaneously emitted power per unit volume coupled with the guided mode can then be written [11] as follows:

$$\begin{aligned} |S(z, \omega)|^2 &= \sum_{i=1}^N \sum_{\substack{m= \\ GS, ES_1}}^N |S_{im}(z, \omega)|^2 \\ &= \beta_{sp} \frac{N_D N_l}{h_W} \sum_{i=1}^N \sum_{\substack{m= \\ GS, ES_1}}^N G_i D_m \frac{\rho_{im}(z, t)}{\tau_m^{sp}} \frac{\Gamma}{\pi} \frac{\hbar \bar{\omega}_{im}}{\Gamma^2 + (\omega - \bar{\omega}_{im})^2} \end{aligned} \quad (5)$$

where τ_m^{sp} is the spontaneous emission characteristic time, which can be directly related to the coefficient A_m [14], N_l represents the number of QD layers, and β_{sp} is the spontaneous emission factor describing the coupling between the spontaneously emitted radiation and the waveguide mode.

Equations (3)–(5) represent therefore a complete description of the linear optical properties of the QD active medium.

The dynamics of exciton populations in the QDs, however, induces significant nonlinearities in the polarization. In order to properly describe population dynamics in the QDs, a set of multi-population rate equations [13] will be considered and described in Sections II-C and II-D.

B. Travelling-Wave Equations

In order to numerically solve the wave (1) taking into account the expressions for the QD polarization (3) and (4), suitable approximations must be introduced.

Following a common approach, the slowly varying envelope approximation is introduced. The mode amplitude $E(z, t)$ is decomposed in forward- and backward-propagating field envelopes $E^\pm(z, t)$, according to

$$E(z, t) = \sqrt{\frac{\mu_0 \omega_0}{k_0}} \left(E^+(z, t) e^{-jk_0 z} + E^-(z, t) e^{+jk_0 z} \right) e^{+j\omega_0 t} \quad (6)$$

where ω_0 is a reference frequency and $k_0 = \omega_0 \eta / c$ is the corresponding reference wave number. A proper normalization has been introduced such that $|E^+(z, t)|^2$ and $|E^-(z, t)|^2$ simply give the total power flowing forward and backward in a given longitudinal section of the device.

Replacing (6) in (1), assuming, $|\partial^2 E^\pm / \partial t^2| \ll |\omega_0 \partial E^\pm / \partial t|$ and $|\partial^2 E^\pm / \partial z^2| \ll |k_0 \partial E^\pm / \partial z|$, one obtains [12]

$$\begin{aligned} \frac{\eta}{c} \frac{\partial E^\pm}{\partial t} \pm \frac{\partial E^\pm}{\partial z} &= -\frac{\alpha_i}{2} E^\pm(z, t) + S^\pm(z, t) - j \frac{\omega_0}{2c\eta} \\ &\times \int_{-\infty}^t \tilde{\chi}(\{\rho_{im}(z, t)\}, t - \tau) E^\pm(z, \tau) d\tau \end{aligned} \quad (7)$$

where we explicitly took into account the intrinsic waveguide losses α_i ; $\tilde{\chi}$, S^\pm are modified expressions for the QD optical susceptibility and spontaneous emission noise source

$$\tilde{\chi} = \chi \times e^{-j\omega_0 t} \quad (8)$$

$$S^\pm = \frac{1}{2} \sqrt{\frac{\mu_0 \omega_0}{k_0}} J_S \times e^{-j\omega_0 t}. \quad (9)$$

In the case of a simple Fabry–Pérot cavity, boundary conditions for (7) can be simply written as follows:

$$E^+(0, t) = r_0 E^-(0, t) \quad (10)$$

$$E^-(L, t) = r_L E^+(L, t) \quad (11)$$

where L is the total cavity length and r_0, r_L are the modal reflectivities at the left and right facet of the device, respectively.

The reference frequency ω_0 is usually chosen close to the lasing frequency. As already pointed out, however, the important role played by the ES contributions to the QD optical susceptibility requires that a large bandwidth, covering both GS and ES characteristic transition energies, is considered. The reference frequency is therefore chosen as the central frequency between the GS and the ES transition of the QD population with the highest existence probability: $\omega_0 = (\bar{\omega}_{(N+1)/2, ES_1} + \bar{\omega}_{(N+1)/2, GS})/2$, as depicted in Fig. 1(c) and (d). Within this choice, the validity of (7) must be verified: InAs QDs emitting at 1.3 μm have energy differences between GS and ES interband transitions of about 60 meV [7]; assuming GS lasing and with the chosen reference frequency, the detuning $\Delta\omega$ between the lasing frequency and ω_0 would be about 7.5 THz whereas ω_0 would be about 249 THz. The ratio $\Delta\omega/\omega_0 \approx 3\% \ll 1$ ensures that the slowly varying envelope approximation can still be applied, preserving a good accuracy of the final solution.

Equation (7) can be solved numerically via a finite difference scheme. Δz being the unit step of a longitudinal discretization of the laser cavity and defining $\tilde{\omega} = \omega - \omega_0$, the solution of (7) in frequency domain can be approximated as follows:

$$\begin{aligned} E^\pm(z \pm \Delta z, \tilde{\omega}) &\cong \exp\left(-j\eta \frac{\tilde{\omega}}{c} \Delta z\right) \\ &\times \left\{ 1 - j \frac{\omega_0}{2c\eta} \tilde{\chi}(\tilde{\omega}, z) \Delta z \right\} E^\pm(\tilde{\omega}, z) + \Delta z S^\pm(\tilde{\omega}, z). \end{aligned} \quad (12)$$

Coming back in time-domain, we obtain

$$\begin{aligned} E^\pm(z \pm \Delta z, t + \Delta t) \\ \cong E^\pm(z, t) - j P^\pm(z, t) \Delta z + S^\pm(z, t) \Delta z - \frac{\alpha_i}{2} E^\pm(z, t) \Delta z \end{aligned} \quad (13)$$

where $\Delta t = \Delta z \eta / c$ is the simulation time step and where we defined a new slowly varying effective polarization

$$P^\pm(z, t) = \frac{\omega_0}{2c\eta} \int_{-\infty}^t \tilde{\chi}(z, t - \tau) E^\pm(\tau, z) d\tau. \quad (14)$$

The convolution integral in (14) must be evaluated numerically. Using (4) and (8), an explicit expression for $\tilde{\chi}(z, t)$ in time-domain can be found. Introducing it in (14), $P^\pm(z, t)$ can finally be expressed as the sum of single GS and ES contributions from each QD population

$$P^\pm(z, t) = \sum_{i=1}^N \sum_{\substack{m= \\ GS, ES_1}} p_{im}^\pm(z, t) \quad (15)$$

where each contribution p_{im}^\pm is written in time-domain as

$$p_{im}^\pm(z, t) = \frac{j}{\hbar} \frac{\omega_0}{2\pi c\eta} \frac{\Gamma_{xy}}{h_W} N_D G_i A_m D_m (2\rho_{im}(z, t) - 1) \times I_{im}^\pm(z, t) \quad (16)$$

with

$$I_{im}^\pm(z, t) = \int_{-\infty}^t e^{j(\bar{\omega}_{im} - \omega_0)(t-\tau)} e^{-\Gamma(t-\tau)} E^\pm(z, \tau) d\tau. \quad (17)$$

In expressions (16) and (17), the dynamics of the carrier occupation probability ρ_{im} has been treated adiabatically. In order to numerically compute the convolution integral (17), a closed form can be found as follows:

$$I_{im}^\pm(z, t) = e^{j(\bar{\omega}_{im} - \omega_0)\Delta t} e^{-\Gamma\Delta t} I_{im}^\pm(z, t - \Delta t) + \frac{1}{2}\Delta t \left[E^\pm(z, t) + e^{j(\bar{\omega}_{im} - \omega_0)\Delta t} e^{-\Gamma\Delta t} E^\pm(z, t - \Delta t) \right]. \quad (18)$$

Finally, a suitable expression for the spontaneous emission noise source $S^\pm(z, t)\Delta z$ appearing in (13) must be considered. This term can be represented as a random process having a power spectral density per unit volume given by (5). Following an approach similar to the one described in [15], a realization of this random process can be obtained via the expression as follows:

$$S^\pm(z, t)\Delta z = \sum_{i=1}^N \sum_{\substack{m= \\ GS, ES_1}} \left[\Gamma \sqrt{\frac{\hbar \bar{\omega}_{im}}{\pi \Gamma \Delta t}} \frac{\beta_{sp} N_{im}(z, t)}{2\tau_m^{sp}} I_{im}^{sp\pm}(z, t) \right] \quad (19)$$

with

$$I_{im}^{sp\pm}(z, t) = \int_{-\infty}^t e^{j(\bar{\omega}_{im} - \omega_0)(t-\tau)} e^{-\Gamma(t-\tau)} e^{j\varphi_{im}(z, \tau)} d\tau \quad (20)$$

where $\varphi_{im}(z, t)$ is a set of independent random phase contributions uniformly distributed between 0 and 2π and completely uncorrelated both in time and space.

In (19), $N_{im}(z, t)$ represents the total number of carriers occupying the m th state in QDs belonging to the i th population and lying within the longitudinal slice of the cavity $[z - \Delta z/2, z + \Delta z/2]$

$$N_{im}(z, t) = N_i N_D G_i D_m \rho_{im}(z, t) W \Delta z \quad (21)$$

where W is the ridge width.

The convolution integral (20) can be evaluated numerically in the same way as (18) where the modal field amplitude is substituted with the random phase term $e^{j\varphi_{im}(t, z)}$ as follows:

$$I_{im}^{sp\pm}(z, t) = e^{j(\bar{\omega}_{im} - \omega_0)\Delta t} e^{-\Gamma\Delta t} I_{im}^{sp\pm}(z, t - \Delta t) + \frac{1}{2}\Delta t \left[e^{j\varphi_{im}(z, t)} + e^{j(\bar{\omega}_{im} - \omega_0)\Delta t} e^{-\Gamma\Delta t} e^{j\varphi_{im}(z, t - \Delta t)} \right]. \quad (22)$$

Equations (13) and (15)–(22), together with boundary conditions (10) and (11) can therefore completely describe the field propagation in the cavity provided that the coupled temporal dynamics of the carrier occupation probabilities in the QD states is determined in each longitudinal slice. The model must therefore be able to properly describe carrier dynamics in each longitudinal section of the waveguide. Dedicated rate equation systems for carrier dynamics in forward-biased gain sections and reverse-biased saturable absorber sections will be therefore considered and separately described in the following paragraphs.

C. Carrier Dynamics in Gain Sections

The set of rate equations to be solved in each forward-biased longitudinal slice of the device consists of one equation for each QD confined state of each QD group, an equation for the total number of carriers in the 2-D QW states, and one for the total number of carriers in the SCH states.

The complete system of equations for a given longitudinal slice of the waveguide under current injection [13], [16] reads as follows:

$$\frac{dN_{SCH}}{dt} = \eta_i \frac{J}{e} \Delta z W - \frac{N_{SCH}}{\tau_r^{SCH}} - \frac{N_{SCH}}{\tau_c^W} + \frac{N_W}{\tau_e^W} \quad (23a)$$

$$\frac{dN_W}{dt} = \frac{N_{SCH}}{\tau_c^W} - \frac{N_W}{\tau_e^W} - \frac{N_W}{\tau_r^W} - \sum_{i=1}^N \frac{G_i}{\tau_c} N_W (1 - \rho_{iES_2}) + \sum_{i=1}^N \frac{N_{iES_2}}{\tau_e^{ES_2}} \quad (23b)$$

$$\frac{dN_{iES_2}}{dt} = \frac{G_i}{\tau_c^{ES_2}} N_W (1 - \rho_{iES_2}) - \frac{N_{iES_2}}{\tau_e^{ES_2}} - \frac{N_{iES_2}}{\tau_s^{ES_2}} - \frac{N_{iES_2} \rho_{iES_2}}{\tau_{Au}^{ES_2}} - \frac{N_{iES_2}}{\tau_c^{ES_1}} (1 - \rho_{iES_1}) + \frac{N_{iES_1}}{\tau_e^{ES_1}} (1 - \rho_{iES_2}) \quad (23c)$$

$$\frac{dN_{iES_1}}{dt} = \frac{N_{iES_2}}{\tau_c^{ES_1}} (1 - \rho_{iES_1}) - \frac{N_{iES_1}}{\tau_e^{ES_1}} (1 - \rho_{iES_2}) - \frac{N_{iES_1} \rho_{iES_1}}{\tau_{Au}^{ES_1}} - \frac{N_{iES_1}}{\tau_c^{GS}} (1 - \rho_{iGS}) + \frac{N_{iGS}}{\tau_e^{GS}} (1 - \rho_{iES_1}) - \frac{N_{iES_1}}{\tau_s^{ES_1}} - \frac{j\Delta z}{\hbar \bar{\omega}_{iES_1}} \left[\left(E^+ p_{iES_1}^{+*} - E^{+*} p_{iES_1}^+ \right) + \left(E^- p_{iES_1}^{-*} - E^{-*} p_{iES_1}^- \right) \right] \quad (23d)$$

$$\begin{aligned} \frac{dN_{iGS}}{dt} = & \frac{N_{iES_1}}{\tau_c^{GS}} (1 - \rho_{iGS}) - \frac{N_{iGS}}{\tau_e^{iGS}} (1 - \rho_{iES_1}) \\ & - \frac{N_{iGS}}{\tau_s^{GS}} - \frac{N_{iGS}\rho_{iGS}}{\tau_{Au}^{GS}} \\ & - \frac{j\Delta z}{\hbar\bar{\omega}_{iGS}} \left[\left(E^+ p_{iGS}^+ - E^{+*} p_{iGS}^+ \right) \right. \\ & \left. + \left(E^- p_{iGS}^- - E^{-*} p_{iGS}^- \right) \right] \end{aligned} \quad (23e)$$

where the total number of electron-hole pairs N_{im} in the m th QD state of the i th QD population is related to the corresponding occupation probability via (21), J is the applied current density, η_i is the internal quantum efficiency, and, finally, N_{SCH} and N_W are the total number of carriers in the SCH and QW.

The characteristic capture times τ_c^W and $\tau_c^{ES_2}$ describe the carrier relaxation from the SCH states to the QW states and from the QW to the upper QD ES, respectively. In the case of a forward-biased section, the value of τ_c^W is chosen as the sum of the characteristic time for carrier diffusion across the SCH region and the carrier capture time in the QW states. The characteristics times τ_c^m with $m = GS, ES_1$ describe carrier relaxation within the QDs. Finally, τ_{Au}^m with $m = GS, ES_1, ES_2$ represent the characteristic Auger recombination times from the QD states.

To guarantee the recovery of a quasi equilibrium energy distribution under no external perturbations, the escape times are calculated from capture and relaxation times [13] as follows:

$$\tau_e^W = \tau_c^W \frac{DOS_W N_l}{DOS_{SCH} h_{SCH}} \exp\left(\frac{\Delta E_{SCH-W}}{k_B T}\right) \quad (24a)$$

$$\tau_e^{iES_2} = \tau_c^{iES_2} \frac{\mu_{ES_2} N_D}{DOS_W} \exp\left(\frac{\Delta E_{W-iES_2}}{k_B T}\right) \quad (24b)$$

$$\tau_e^{iES_1} = \tau_c^{iES_1} \frac{DES_1}{DES_2} \exp\left(\frac{\hbar\bar{\omega}_{iES_2} - \hbar\bar{\omega}_{iES_1}}{k_B T}\right) \quad (24c)$$

$$\tau_e^{iGS} = \tau_c^{iGS} \frac{DGS}{DES_1} \exp\left(\frac{\hbar\bar{\omega}_{iES_1} - \hbar\bar{\omega}_{iGS}}{k_B T}\right) \quad (24d)$$

where ΔE_{SCH-W} is the energy difference between SCH and QW band edges and ΔE_{W-iES_2} are the energy difference between the QW band edge and the highest energy confined states in the various QD groups; h_{SCH} is the SCH width, and DOS_W and DOS_{SCH} are the effective density of states in the QW and in the SCH, respectively [13] as follows:

$$DOS_{SCH} = 2 \left(2 \frac{\pi m_{SCH}^* k_B T}{\hbar^2} \right)^{\frac{3}{2}} \quad (25a)$$

$$DOS_W = \frac{m_W^* k_B T}{\pi \hbar^2} \quad (25b)$$

where m_{SCH}^* and m_W^* are the exciton effective masses in the GaAs SCH and InGaAs QW, respectively.

Equations (23a)–(23e) represent therefore the complete set of equations to be solved to determine the carrier dynamics in each section of the cavity under current injection. Coupling with the field propagation is given in (23d) and (23e) by the stimulated emission terms involving polarizations p_{im}^\pm .

D. Carrier Dynamics in Saturable Absorber Sections

In order to properly take into account the effects of a static transverse electric field on the carrier dynamics in a reverse-biased saturable absorber section, a dedicated set of rate equations must be solved.

Enhanced thermionic escape rates from the QD states to the WL and SCH states due to barrier reduction and additional escape paths due to tunneling processes toward the SCH were found to be the main effects influencing the carrier dynamics under an applied electric field [3], [17]. A weak quantum confinement Stark effect in QD structures has been also observed when compared with QW structures [17]. This latter effect is therefore neglected in the model, whereas the influence of the applied field on both thermionic and tunneling escape processes will be properly introduced using simple approaches.

An expression for the tunneling escape rates from the QD states and the QW to the 3-D states in the SCH can be estimated using the Wentzel–Kramer–Brillouin approximation for a triangular well [3] as follows:

$$R_{tun}^k = f_{tun}^k e^{\left(-\frac{4}{3} \sqrt{2m_{SCH}^*} \frac{(\Delta E_{SCH-k})^{\frac{3}{2}}}{eh} \frac{h_{SCH}}{V+V_{bi}} \right)} N_k \quad (26)$$

where index $k = \{im\}$, W runs over the complete set of QD states and the QW, ΔE_{SCH-k} is the energy difference between the SCH band edge and the k th confined state, f_{tun}^k is the characteristic barrier collision frequency for carriers in the QDs and QW, $V \geq 0$ is the reverse voltage applied across the p-i-n junction and V_{bi} is the built-in potential of the junction (a constant electric field $(V + V_{bi})/h_{SCH}$ in the active region has been assumed).

The enhanced thermionic escape rate from the QD states to the QW and from the QW to the SCH states, due to a linear barrier reduction induced by the applied electric field, can then be simply modeled via modified expressions for the characteristic escape times [3] as follows:

$$\tau_e^{iES_2}(V) = \tau_e^{iES_2} \exp\left(-\frac{V + V_{bi}}{k_B T} \frac{h_W}{2h_{SCH}}\right) \quad (27a)$$

$$\tau_e^W(V) = \tau_e^W \exp\left(-\frac{V + V_{bi}}{k_B T} \frac{h_W}{2h_{SCH}}\right) \quad (27b)$$

where τ_e^W , $\tau_e^{iES_2}$ are the escape times calculated at zero electric field via expressions (24a) and (24b).

Finally, for reverse-biased saturable absorber sections, we introduce a modified rate equation for carriers in the SCH as follows:

$$\begin{aligned} \frac{dN_{SCH}}{dt} = & -\mu_d N_{SCH} \frac{V + V_{bi}}{h_{SCH}^2} - \frac{N_{SCH}}{\tau_{nr}^{SCH}} \\ & - \frac{N_{SCH}}{\tau_c^W} + \frac{N_W}{\tau_e^W} + \sum_{k=\{im\}, W} R_{tun}^k \end{aligned} \quad (28)$$

where the first term on the right-hand side represents the electron drift current, μ_d being the GaAs electron mobility. Adding the expressions for the tunneling escape rates (26) in (23b)–(23e), introducing the field-dependent escape rates (27a) and (27b) in (23b) and (23c), and replacing (23a) with (28),

one obtains therefore a complete set of equations describing the carrier dynamics in a QD saturable absorber section.

E. Choice of the Simulation Time Step

Some further comments must be made on the choice of the simulation time step Δt . The unit step must guarantee a good accuracy when performing the numerical solution of the wave equation (13) via the calculation of the polarization terms (15)–(18). The unit step must therefore be small enough so that the whole spectrum of the QD optical susceptibility involving both GS and ES transitions is properly resolved. Moreover, the Lorentzian filters describing the QD optical susceptibility may have tails which are beyond the Nyquist frequency; these contributions introduce aliasing within the simulated bandwidth, which mainly affects the description of the real part of the susceptibility. For the GS–ES separation we are assuming, a time step $\Delta t = 10$ fs has been therefore chosen. In Fig. 1, we compared the theoretical QD gain and refractive index spectra at zero-bias condition with the spectra obtained from the response of the numerical filters. A good agreement between theoretical and numerically computed spectra is achieved, proving that the chosen time step guarantees a good accuracy within a sufficiently large bandwidth.

We must point out that the chosen time step steeply increases the computational time required by the simulations. An exploited alternative to relax the condition on the required time step is to limit the investigated spectral bandwidth over the GS interband transitions, setting $\omega_0 = \bar{\omega}_{(N+1)/2,GS}$ and considering the residual contributions to the QD gain and refractive index spectra at frequencies around ω_0 induced by the ES populations as frequency-independent contributions $\chi_{iES_1}(\rho_{iES_1}, \omega_0)$. Simulations performed with this approach have shown rather good agreement with the results obtained by properly resolving both the GS and ES interband transitions. Using this approach, however, no control over the onset of ES lasing or simultaneous GS and ES lasing can be achieved. Moreover, this approximation may lead to less accurate results when simulating ML lasers exhibiting very short subpicosecond optical pulses.

F. Numerical Model Implementation

In conclusion, in the implemented numerical model, at first a proper discretization of the time axis with unit step Δt is considered; the waveguide is then discretized in its longitudinal direction (z -axis) with unit step Δz . Each longitudinal slice of the cavity is assumed to be either forward- or reverse-biased; in this way, devices with different electrically isolated sections acting as gain sections or saturable absorbers can be properly considered. Once the device structure has been defined, all the model variables are initialized and at each time step the following procedure is performed:

- 1) multi-population rate equations described in Sections II-C and II-D are solved in each longitudinal slice with a first-order finite difference approximation, to obtain the occupation probabilities in the QD states at the current time instant t ;

- 2) the polarization terms $P^\pm(z, t)$ are computed according to (15), (16), and (18);
- 3) values for the spontaneous emission noise sources $S^\pm(z, t)\Delta z$ are generated according to (19) and (20);
- 4) forward and backward travelling fields at the next time step $t + \Delta t$ are then calculated in each slice of the cavity according to (13) and boundary conditions (10) and (11).

The above steps are iteratively repeated to compute the field and carrier dynamics over the whole time interval.

III. FORWARD- AND REVERSE-BIASED QD SOA

Simulations of gain/absorption recovery in QD SOAs at different bias conditions were performed. A comparison with published results of DTS experiments [2], [3] and [17] allowed us a first validation of the model parameters.

A single-mode ridge waveguide SOA with 500- μm total length and 6- μm ridge width is considered. The active region consists of five InGaAs dot-in-a-well layers embedded in a p-i-n heterostructure where an intrinsic GaAs SCH layer between two AlGaAs cladding layers guarantees the optical confinement along the growth direction. Device facets are assumed to be tilted and antireflection (AR) coated, allowing us to consider ideal zero facet reflectivities. The main material and device parameters are summarized in Table I.

In DTS experiments, the gain changes induced by a pump pulse are measured by monitoring the transmission of weak probe pulses with variable delay times relative to the pump. The probe pulse energy is assumed to be small enough such that the gain dynamics is not significantly perturbed. Within this assumption, considering a reference framework moving with the pulse, the single-pass gain experienced by the weak probe pulse can be simply approximated as

$$G(\tau, \omega) = \exp\left(\int_0^L g(z, \tau + z/v_g, \omega) dz - \alpha_i L\right) \quad (29)$$

where v_g is the group velocity of the pulse, L is the waveguide length, g is the net modal gain calculated from the QD optical susceptibility (4), and τ is the time delay between pump and probe pulses. Gain/absorption dynamics induced by the propagation of a pump pulse in a QD SOA under both forward and reverse polarization is studied as a function of the applied bias conditions. In the results presented below, we always considered probe pulses with the same frequency as the frequency of the pump pulse ω_p . Neglecting spectral artifacts related to the finite bandwidth of the probe pulse, the changes in the probe single-pass gain induced by the pump are simply written as $\Delta G(\tau, \omega_p) = G(\tau, \omega_p) - G_0(\omega_p)$ [dB], where $G_0(\omega_p)$ is the single-pass gain experienced by the probe pulse in absence of the pump-induced perturbation (expressed in dB).

An unchirped Gaussian pump pulse with 250 fs width and 1.28 pJ pulse energy, resonant with the GS transition ($\hbar\omega_p = 0.99$ eV) is considered.

Net modal gain spectra for various values of injected current I computed in absence of external optical excitation are shown in Fig. 2(a). The pump-induced changes in the single-pass gain experienced by the probe pulse as a function of the delay time relative to the pump pulse, $\Delta G(\tau, \omega_p)$, are shown in Fig. 2(b) for the same bias currents.

TABLE I
MAIN MODEL PARAMETERS

Symbol	Description	Values	
<i>Material parameters</i>			
h_w	QW width	5 nm	
η	Effective refractive index	3.3445	
N_l	Number of QD layers	5	
N_D	QD surface density	$2.85 \times 10^{10} \text{cm}^{-2}$	
N	Number of QD groups	7	
D_m	State degeneracy $m = ES_2, ES_1, GS$	6, 4, 2	
$\hbar\Gamma$	Homogeneous linewidth	10 meV	
ΔE	FWHM of the inhomogeneous gain broadening	34 meV	
A_m	Dipole matrix element $m = ES_l, GS$	$5.82 \times 10^{-21}, 6.03 \times 10^{-21} \text{cm}^3 \text{eV}$	
τ_c^m	Relaxation times $m = W, ES_2, ES_1, GS$	(24.5 + 0.3), 0.4, 0.3, 0.4 ps	
τ_r^m	Interband recombination times from $m = SCH, W$	100, 100 ps	
τ_s^m	Spontaneous emission recombination times from $m = ES_2, ES_1, GS$	2, 2, 2 ns	
τ_{Au}^m	Auger recombination times from $m = ES_2, ES_1, GS$	110, 275, 660 ps	
β_{sp}	Spontaneous emission coupling factor	1×10^{-4}	
$\hbar\bar{\omega}_{im}$	Interband transition energies for $i = (N + 1)/2; m = ES_2, ES_1, GS$	1.1060, 1.0597, 0.9904 eV	
α_i	Intrinsic waveguide losses	1.5cm^{-1}	
V_{bi}	Built-in potential	0.8 V	
<i>Device parameters</i>			
		SOA	ML LASER
W	Ridge width	6 μm	6 μm
h_{SCH}	SCH width	439 nm	439 nm
r_0^2	SA side power reflectivity	0%	99%
r_L^2	Gain section side power reflectivity	0%	10%
L	Total device length	500 μm	2 mm
L_{abs}	Absorber length	—	350 μm

In the gain regime, the pump pulse strongly depletes carrier populations in the QD GSs resonant with the pulse frequency, leading to a significant gain compression. The maximum gain compression induced by the pump increases significantly with the applied current. Gain dynamics then shows a dominant ultrafast recovery completed in a picosecond time scale, followed by long-lasting changes occurring on a time scale of hundreds of picoseconds and leading to a clear offset in the gain curves within the investigated time interval. This offset significantly reduces with the applied current and it is attributed to changes in the total carrier density in the active region, limited by carrier diffusion across the SCH (τ_c^W).

According to the experimental results shown in [2], the dominant ultrafast gain recovery can be well fitted with a double exponential function $\Delta G(\tau) = A_0 + A_{fast}e^{-\tau/\tau_{fast}} + A_{slow}e^{-\tau/\tau_{slow}}$, where τ_{fast} and τ_{slow} are the characteristic time constants, A_{fast} and A_{slow} are the corresponding amplitudes relative to the total gain compression, and A_0 is an offset accounting for the slow dynamics discussed above. An example of the obtained fitting is shown in the inset of Fig. 2(b). Consistently with DTS experiments published in [2], gain recovery is characterized by an ultrafast time constant τ_{fast} in the range between 300 and 150 fs, and by a slower recovery time τ_{slow} of about 1 ps, both decreasing with increasing current.

We now consider the same device under reverse bias condition, acting therefore as a saturable absorber. We apply a voltage ranging from 0 V (short circuit) to 10 V. The obtained

absorption dynamics is shown in Fig. 2(c) for the different bias values. The absorption of the strong pump pulse causes the generation of carriers in the QD GSs, leading to a significant absorption bleaching. The maximum absorption bleaching induced by the pump pulse decreases slightly with the applied bias, but it is always much larger than the maximum gain compression in the forward-biased SOA, consistently with the expected difference in the differential gain and absorption in forward- and reverse-bias conditions, respectively.

The subsequent absorption recovery can again be well fitted using a double exponential function. At low applied voltages, an initial ultrafast absorption recovery time τ_{fast} ranging from 400 to 300 fs is obtained; this dynamics is associated with the efficient excitation of the photogenerated GS carriers to the higher energy states ES_1 and ES_2 . The amplitude of this ultrafast recovery A_{fast} is, however, significantly smaller than that of the ultrafast component in the SOA gain recovery and decreases further when the applied voltage is increased. The absorption recovery is instead dominated by a slower time constant τ_{slow} , strongly dependent on the applied reverse bias, decreasing from 41 ps at 0 V down to 2.5 ps at 10 V as presented in Fig. 2(d). Simulations show that, at low applied voltages, the dominant time constant τ_{slow} is mainly due to thermionic escape from the QD confined states to the QW states, which allows carrier thermalization among the various QD groups, guaranteeing, in a time scale of tens of picoseconds, the recovery of a quasi-equilibrium energy distribution of carriers in the whole QD ensemble. The absorption recovery

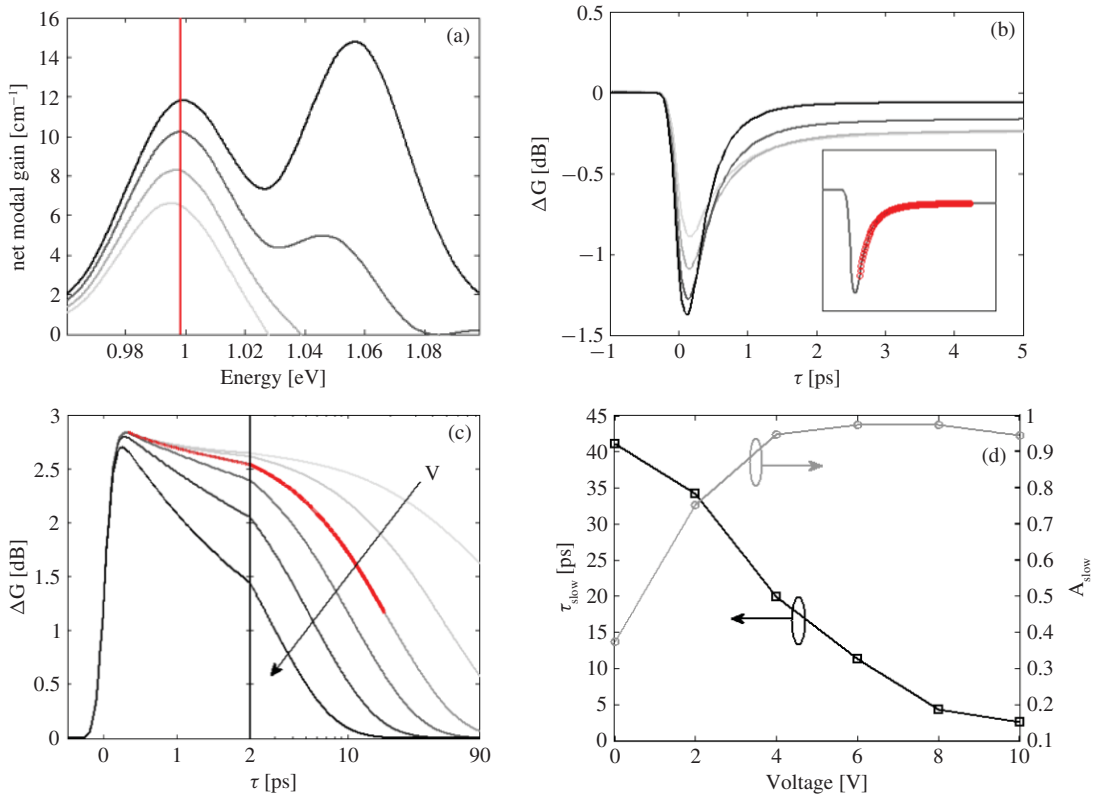


Fig. 2. (a) Gain spectra for the forward-biased QD SOA for current $I = 5, 8, 15, 40$ mA; red vertical line shows the central frequency of the pump pulse. (b) Corresponding gain dynamics induced by the pump pulse, inset: fitting with a double exponential function. (c) Absorption dynamics in the reverse-biased SOA for voltage ranging from 0 V up to 10 V in step of 2 V, time axis is displayed in linear scale up to 2 ps and in logarithmic scale from 2 ps to 90 ps for clarity, bold red line shows fitting with a double exponential for $V = 4$ V. (d) Characteristic time constant of the slow absorption recovery contribution and corresponding amplitude as a function of the applied voltage.

is then completed thanks to nonradiative recombination and spontaneous emission processes occurring on a time scale of hundreds of picoseconds.

On increasing the applied voltage, thermionic escape is enhanced according to (27a) and (27b) but for voltages larger than 5 V, tunneling processes from the QD states toward the 3-D SCH states become the dominant contribution to the absorption recovery, leading to a significant reduction in the recovery time constant τ_{slow} . The described behavior is in good agreement with the absorption recovery measured from DTS experiments [3], [17].

The preliminary study presented in this section and the comparison of the simulation results with published DTS experiments allowed validation of the chosen set of model parameters and gaining insights into the peculiar properties of the QD gain and absorption dynamics, governing the pulse generation in two-section QD passively ML lasers. In the next section, simulations of passive mode-locking in a two-section device with the same active region as the previously simulated SOA will therefore be presented.

IV. PASSIVE MODE-LOCKING

The model is now applied to the simulation of passive mode-locking in a two-section edge-emitting QD laser with 2 mm total length and the same structure as the previously investigated SOA. The laser cavity consists of a 350- μm long reverse-biased saturable absorber (SA) section and a 1650- μm long

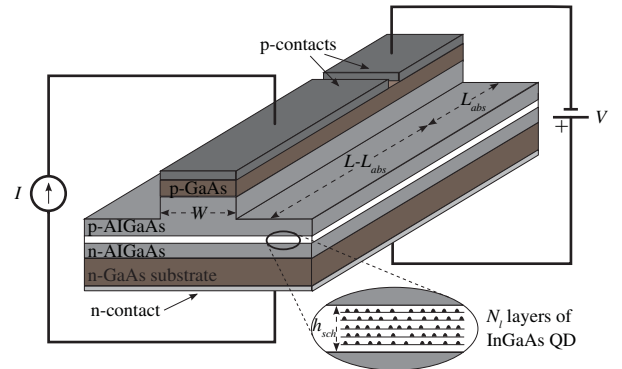


Fig. 3. Schematic of the simulated two-section QD ML laser.

forward-biased gain section. High-reflection (HR) coatings are applied at the absorber facet, leading to a power reflectivity of 99%, while the reflectivity at the output facet is reduced down to 10% by the application of AR coatings. A schematic of such a device is presented in Fig. 3.

The ML regime is investigated as a function of the bias parameters. In the investigated parameter range, lasing always occurs at GS wavelengths. Fig. 4(a) shows the behavior of pulse width and peak power as a function of the current applied in the gain section for a fixed 7 V reverse bias in the SA. Both pulse width and peak power monotonically increase with the applied current; pulse width increases from 7 ps at 200 mA up to 12 ps at 350 mA; the increase in the average optical

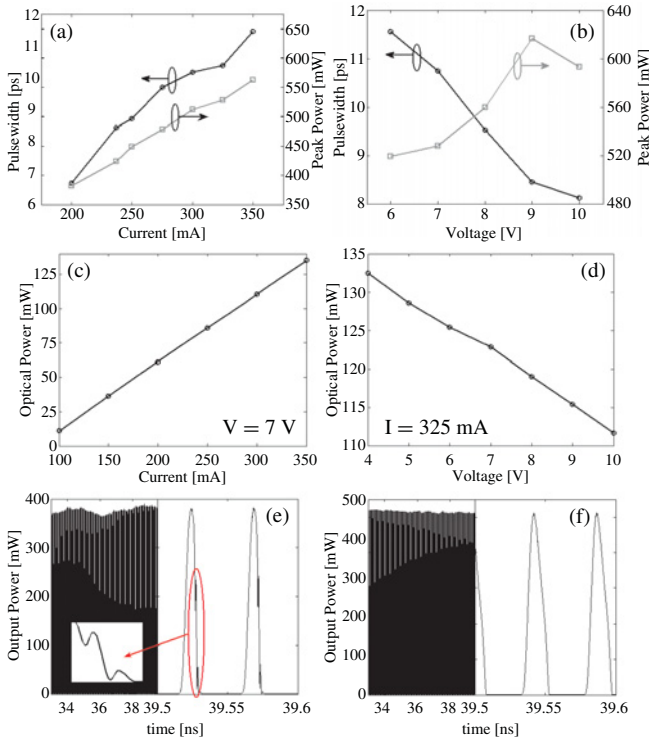


Fig. 4. (a) Pulse width (black) and peak power (gray) as a function of the current injected in the gain section for a fixed 7 V SA voltage. (b) Pulse width (black) and peak power (gray) as a function of the SA reverse voltage for a fixed current $I = 325$ mA. (c) Average power as a function of current for a fixed 7 V SA voltage. (d) Average power as a function of the SA voltage for $I = 325$ mA. (e, f) Time traces of output ML pulse for a fixed $V = 7$ V in the SA and with a current in the gain section of $I = 200$ mA and $I = 325$ mA, respectively. Trailing edge instability in the ML pulses at 200 mA is clearly visible in the inset.

power with current [see Fig. 4(c)] completely compensates the pulse broadening, allowing the peak power to increase almost linearly with current. This behavior is currently observed in QD ML lasers [4]. One must also notice that, by reducing the current below 200 mA toward the laser threshold, the pulse width could be significantly reduced; however, in this current range, low-frequency modulations appear superimposed on the ML pulses and trailing edge instability can be clearly identified in the time trace of the output pulses as shown in Fig. 4(e). The onset of such instability at low current can be well explained by the balance between the gain and absorption dynamics as will be discussed in detail in the following.

Fig. 4(b) then shows the behavior of pulse width and peak power as a function of the applied voltage for a fixed gain current of 325 mA. The ML pulse width significantly decreases with the applied voltage: for voltages close to 0 V, the laser operates in continuous-wave regime; on increasing the reverse bias, incomplete ML is obtained where the trailing edge instability is significantly enhanced; for values larger than 5 V, a stable ML is instead achieved. Pulse width decreases from 11.6 ps at 6 V down to 8 ps at 10 V thanks to the speedup of the absorption recovery in the SA section. The increase in the reverse voltage also increases the stability of the ML regime against trailing-edge instabilities.

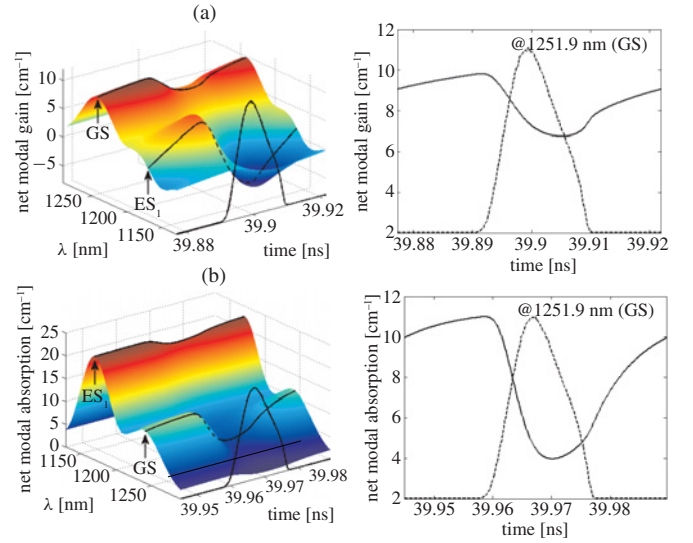


Fig. 5. (a) Left: temporal dynamics of the QD net modal gain spectrum at a fixed $z = 1980 \mu\text{m}$ in the gain section during the passage of a ML pulse; the ML pulse envelope traveling in the considered section is also shown. Black lines highlight the gain dynamics at the center pulse wavelength (1251.9 nm, resonant with GS transitions) and the gain dynamics at the corresponding ES wavelength. Right: Detail of the gain dynamics at the center pulse wavelength (1251.9 nm). (b) Left: Temporal dynamics of the QD net modal absorption spectrum at a fixed $z = 20 \mu\text{m}$ in the SA section during the passage of a ML pulse. Right: Detail of the absorption dynamics at the center pulse wavelength.

The decrease in the pulse width with the applied voltage is accompanied by a significant reduction in the average output power due to the weaker absorption saturation in the SA [Fig. 4(d)]. Up to 9 V, the decrease in the pulse width with the applied voltage is larger than the decrease in the average power, leading to a significant increase in the pulse peak power. On the contrary, for voltages larger than 9 V, the decrease in the pulse width becomes weaker compared to the corresponding reduction in the average power and the peak power starts to decrease.

In order to gain insights into the onset of the described ML regime, we considered two fixed longitudinal sections of the device in the SA section, at $z = 20 \mu\text{m}$, close to the absorber facet, and in the gain section, at $z = 1980 \mu\text{m}$, close to the output laser facet. Fig. 5(a) and (b) shows the temporal dynamics of the net modal gain spectrum and net modal absorption spectrum induced by the passage of a ML pulse in the considered sections, at 325 mA and 7 V.

As expected, the maximum absorption bleaching in the SA induced by the ML pulse with a center wavelength of 1251.9 nm, which is resonant with the GS transitions, is significantly larger than the maximum gain compression in the gain section, due to the large difference between the gain and absorption saturation energies.

In the gain section, during the pulse trailing edge, an initial ultrafast recovery of the net modal gain at the GS wavelength can be clearly identified; such a behavior can be directly correlated to the subpicosecond recovery time constant obtained from DTS experiments, as discussed in the previous section [Fig. 2(b)], and attributed to the fast carrier energy relaxation from the ES to the GS.

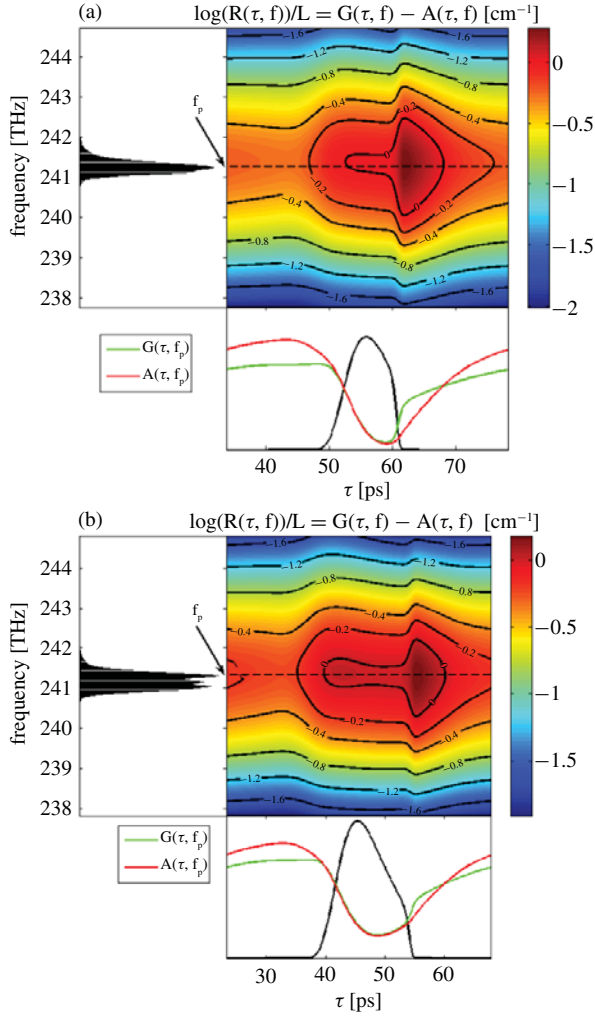


Fig. 6. Map of the normalized round trip gain spectra $\ln(R(\tau, f))/L = G(\tau, f) - A(\tau, f)$, experienced by a ML pulse for a gain current of (a) 235 mA and (b) 325 mA, respectively, at a fixed 7 V reverse bias. Optical spectrum of the obtained steady-state ML pulses in linear scale is displayed in the left part of each figure. At the bottom of each figure, the corresponding time trace of the pulse power is shown together with single contributions to the total round-trip gain due to amplification in the gain section $G(\tau, f_p)$, and saturable and non-saturable losses in the cavity $A(\tau, f_p)$ evaluated at the peak frequency of the optical spectrum f_p .

Such ultrafast dynamics induces also significant changes in the ES populations, leading to a fast decrease in the net modal gain at the corresponding ES wavelengths.

Gain dynamics at the GS wavelength is then completed with a much slower recovery on a time scale of tens of picoseconds which can be related to changes in the total carrier density in the QD active layers, identified as an offset in the simulations of DTS experiments shown in Fig. 2(b).

As shown in Fig. 5(b), the absorption recovery in the SA section, however, does not show any initial ultrafast dynamics during the pulse trailing edge and it is dominated by a picosecond recovery rate mainly attributed to efficient tunneling processes from the QD states to the SCH states.

We must point out that such a difference between the initial ultrafast gain recovery and the picosecond absorption recovery in the SA section represents the main cause for the instability

of the ML regime appearing at low currents, as will be clarified in the following paragraph.

In order to perform a rigorous study of the stability of the steady-state ML regime, we calculated the round-trip gain experienced by a ML pulse after a single round trip in the cavity. To do so, we considered a reference framework moving with the ML pulse so that variables (z, t) are mapped in (z', τ) according to the transformation as follows:

$$\begin{cases} z = z' \\ t = \tau \pm \frac{z'}{v_g} \end{cases} \quad (30)$$

where v_g is the group velocity of the ML pulse and the sign change in (30) takes into account whether the pulse is traveling in the direction $+z$ or $-z$, respectively.

The gain experienced by a ML pulse during a single round trip in the cavity, $R(\tau, \omega)$, can therefore be simply written as

$$R(\tau, \omega) = r_0 r_L \exp\left(\int_0^L (g^+(z, \tau, \omega) + g^-(z, \tau, \omega)) dz\right) \times e^{-\alpha_i L} \quad (31)$$

where $g^+(z, \tau, \omega)$ and $g^-(z, \tau, \omega)$ are the gain experienced by the pulse when traveling along the direction $+z$ and $-z$, respectively. The spatiotemporal evolution of such gain spectra can be simply calculated from the dynamics of the QD optical susceptibility (4) as outlined in Section II-A. We can therefore write

$$\begin{aligned} \ln R(\tau, \omega) &= \int_0^{L_{abs}} (g^+(z, \tau, \omega) + g^-(z, \tau, \omega)) dz \\ &+ \int_{L_{abs}}^L (g^+(z, \tau, \omega) + g^-(z, \tau, \omega)) dz - \alpha_i L - \alpha_m L \end{aligned} \quad (32)$$

where $\alpha_m = \ln(1/(r_0 r_L))/L$ are the mirror losses and where we separated the contributions coming from the SA section ($0 < z < L_{abs}$) and the gain section ($L_{abs} < z < L$). Finally, we define

$$\ln R(\tau, \omega)/L = G(\tau, \omega) - A(\tau, \omega) \quad (33)$$

where

$$A(\tau, \omega) = -\frac{1}{L} \int_0^{L_{abs}} (g^+(z, \tau, \omega) + g^-(z, \tau, \omega)) dz + \alpha_i + \alpha_m \quad (34)$$

$$G(\tau, \omega) = \frac{1}{L} \int_{L_{abs}}^L (g^+(z, \tau, \omega) + g^-(z, \tau, \omega)) dz \quad (35)$$

so that the round trip gain experienced by the pulse can finally be simply written as $R(\tau, \omega) = \exp((G(\tau, \omega) - A(\tau, \omega))L)$.

In Fig. 6(a) and (b), maps of the normalized round trip gain $\ln R(\tau, \omega)/L = G(\tau, \omega) - A(\tau, \omega)$ experienced by the

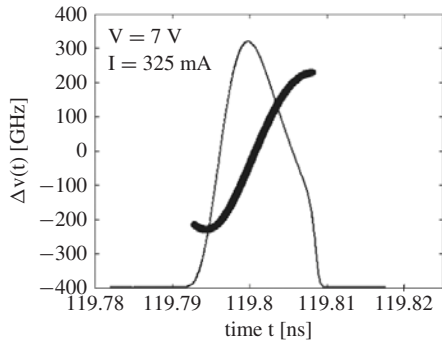


Fig. 7. Instantaneous frequency variation versus time at 7 V reverse bias and $I = 325$ mA.

ML pulse during the propagation in the cavity are shown for 7 V reverse bias and gain currents of (a) 235 mA and (b) 325 mA, respectively. In Fig. 6(a) and (b), the optical spectrum and the time trace of the ML pulse at $z = 0$ are also shown. As expected, the time trace of the ML pulse and its corresponding optical spectrum are significantly different from zero only in a temporal and spectral window where $\ln R(\tau, \omega)/L \geq 0$, i.e., there is a positive net gain per round trip.

According to New's condition [18], a stable ML regime could be achieved only when the net gain window is immediately closed before and after the ML pulse envelope. However, at both bias conditions shown in Fig. 6(a) and (b), a region of positive gain can be clearly identified also immediately after the ML pulse. Such a condition is attributed to the initial ultrafast component in the gain recovery described above. This point can be further clarified by looking at the partial contributions to the overall pulse round-trip gain due to the pulse propagation in the gain section $G(\tau, \omega)$ and to the saturable and non-saturable losses in the cavity $A(\tau, \omega)$, respectively. At the bottom of each map in Fig. 6(a) and (b), superimposed on the ML pulse envelope, partial contributions evaluated at the peak pulse frequency f_p are shown. $G(\tau, 2\pi f_p)$ shows a faster recovery, during the pulse trailing edge, with respect to the recovery of $A(\tau, 2\pi f_p)$, causing the formation of a net gain window extending beyond the pulse duration.

Under this condition, following New's criteria, the noise generated just after the pulse trailing edge could therefore be amplified, leading to instabilities in the obtained ML regime. Despite the qualitative information provided by New's criteria, however, the possibility to achieve a stable ML regime with pulse width much shorter than the overall duration of the net gain window has been demonstrated [19], [20]. As a matter of fact, only the noise generated in the short time window and finite spectral bandwidth corresponding to the net gain region following the pulse can induce a trailing-edge instability of the ML pulses; if the perturbations induced by the spontaneous emission noise are too weak to be significantly amplified during a round trip, a stable ML regime can be safely preserved. Furthermore, differences between the group velocities of the ML pulse and the background noise can further improve the stability of the ML regime. According to this picture, as shown in Fig. 4, stable ML can therefore

be obtained despite the existence of a region of net gain immediately following the ML pulse.

However, as clearly shown in Fig. 6, by decreasing the gain current, the region of net gain exceeding the pulse duration becomes significantly larger; furthermore, also the spectral width of the positive gain region just after the pulse tends to significantly increase when decreasing current. For currents smaller than 200 mA, the amplification of noise following the pulse becomes therefore strong enough to induce the trailing edge instabilities shown in Fig. 4(e).

One final comment must be made on the chirp of the ML pulses. In Fig. 7, a typical behavior of the instantaneous frequency variation of a ML pulse at 7 V and 325 mA is shown. A positive linear chirp of the ML pulse is obtained. The pulse chirp mainly arises from the self-phase modulation induced by the dynamics of the ES populations in both the gain and the SA section [13]. As a matter of fact, even though the ES populations poorly contribute to the stimulated emission processes responsible for pulse amplification and attenuation in the gain and SA sections, their dynamics significantly influences the changes in the refractive index at the lasing wavelengths, leading to a nonzero chirp of the ML pulses, as shown in Fig. 7.

V. CONCLUSION

We developed a finite difference time-domain traveling-wave model including a detailed description of the QD optical susceptibility, spontaneous emission noise, and QD population dynamics.

Preliminary simulations of DTS experiments in forward- and reverse-biased SOA allowed the determination of the peculiar properties of gain and absorption dynamics induced by the QD active layers. Furthermore, comparison with DTS experiments in similar structures allowed a first validation of the model parameters. Consistent with the experiments, the ultrafast gain recovery in a forward-biased SOA was found to be characterized by two different characteristic time constants in the subpicosecond and picosecond range, respectively. In the reverse-biased SOA, absorption recovery was instead found to be dominated by a picosecond recovery time, which was strongly dependent on the applied reverse bias due to enhanced thermionic escape rates and tunneling processes from the QD states.

The model was then applied to investigate the ML regime in a two-section QD laser structure as a function of the bias parameters, i.e., saturable absorber reverse voltage and current in the gain section. Details of the gain and absorption dynamics leading to the generation of the ML pulses were given. The appearance of low-frequency modulation and trailing-edge instability in the ML regime at low current was observed. The instability was attributed to the initial ultrafast gain recovery found in DTS experiments, leading to a net gain window exceeding beyond the pulse duration. This observation was fully supported by a detailed calculation of the total amplification and losses experienced by a ML pulse during a single round trip in the cavity.

Finally a linear frequency chirp of the ML pulses was found and attributed to the refractive index changes induced by the ES population dynamics in the QDs.

REFERENCES

- [1] M. Sugawara, *Self-Assembled InGaAs/GaAs Quantum Dots, Semiconductors and Semimetals*. San Diego, CA: Academic, 1999.
- [2] P. Borri, S. Schneider, W. Langbein, and D. Bimberg, "Ultrafast carrier dynamics in InGaAs quantum dot materials and devices," *J. Pure Appl. Opt. A*, vol. 8, no. 4, pp. S33–S46, 2006.
- [3] D. B. Malins, A. Gomez-Iglesias, S. J. White, W. Sibbett, A. Miller, and E. U. Rafailov, "Ultrafast electroabsorption dynamics in an InAs quantum dot saturable absorber at 1.3 μm ," *Appl. Phys. Lett.*, vol. 89, no. 17, pp. 171111-1–171111-3, Oct. 2006.
- [4] M. G. Thompson, A. R. Rae, M. Xia, R. V. Penty, and I. H. White, "InGaAs quantum-dot mode-locked laser diodes," *IEEE J. Sel. Topics Quantum Electron.*, vol. 15, no. 3, pp. 661–672, May–Jun. 2009.
- [5] Y.-C. Xin, V. Kovanis, A. L. Gray, L. Zhang, and L. F. Lester, "Reconfigurable quantum dot monolithic multisection passive mode locked lasers," *Opt. Exp.*, vol. 15, no. 12, pp. 7623–7633, Jun. 2007.
- [6] G. Fiol, C. Meuer, H. Schmeckeber, D. Arsenijevic, S. Liebich, M. Laemmlin, M. Kuntz, and D. Bimberg, "Quantum-dot semiconductor mode-locked lasers and amplifiers at 40 GHz," *IEEE J. Quantum Electron.*, vol. 45, no. 11, pp. 1429–1435, Nov. 2009.
- [7] E. U. Rafailov, M. A. Cataluna, and W. Sibbett, "Mode-locked quantum-dot lasers," *Nat. Photon.*, vol. 1, pp. 395–401, Jul. 2007.
- [8] E. A. Viktorov, P. Mandel, M. Kuntz, G. Fiol, D. Bimberg, A. G. Vladimirov, and M. Wolfram, "Stability of the modelocking regime in quantum dot laser," *Appl. Phys. Lett.*, vol. 91, no. 23, pp. 231116-1–231116-3, Dec. 2007.
- [9] G. Carpintero, M. G. Thompson, R. V. Penty, and I. H. White, "Low noise performance of passively mode-locked 10-GHz quantum-dot laser diode," *IEEE Photon. Technol. Lett.*, vol. 21, no. 6, pp. 389–391, Mar. 2009.
- [10] A. E. Viktorov, P. Mandel, A. G. Vladimirov, and U. Bandelow, "Model for mode-locking of quantum dot lasers," *Appl. Phys. Lett.*, vol. 88, no. 20, pp. 201102-1–201102-3, 2006.
- [11] C. Xing and E. A. Avrutin, "Multimode spectra and active mode-locking potential of quantum dot lasers," *J. Appl. Phys.*, vol. 97, no. 10, pp. 104301-1–104301-9, May 2005.
- [12] U. Bandelow, M. Radziunas, A. Vladimirov, B. Hüttel, and R. Kaiser, "40 GHz mode-locked semiconductor lasers: Theory, simulations and experiment," *Opt. Quantum Electron.*, vol. 38, nos. 4–6, pp. 495–512, Mar. 2006.
- [13] M. Gioannini and I. Montrosset, "Numerical analysis of the frequency chirp in quantum-dot semiconductor lasers," *IEEE J. Quantum Electron.*, vol. 43, no. 10, pp. 941–949, Oct. 2007.
- [14] P. Bardella, M. Rossetti, and I. Montrosset, "Modeling of broadband chirped quantum-dot super-luminescent diodes," *IEEE J. Sel. Topics Quantum Electron.*, vol. 15, no. 3, pp. 785–791, May–Jun. 2009.
- [15] J. E. Carroll, J. Whiteaway, and R. Plumb, *Distributed Feedback Semiconductor Lasers*. London, U.K.: IEE SPIE Press, 1998.
- [16] F. Boxberg, J. Tulkki, G. Yusa, and H. Sakaki, "Cooling of radiative quantum-dot excitons by terahertz radiation: A spin-resolved Monte Carlo carrier dynamics model," *Phys. Rev. B*, vol. 75, p. 115334, Mar. 2007.
- [17] M. G. Thompson, C. Marinelli, Y. Chu, R. L. Sellin, R. V. Penty, I. H. White, M. Van Der Poel, D. Bikedal, J. Hvam, V. M. Ustinov, M. Lammlin, and D. Bimberg, "Properties of InGaAs quantum dot saturable absorbers in monolithic mode-locked lasers," in *Proc. 19th Int. Semicond. Laser Dig. Conf.*, Sep. 25, 2004, pp. 55–54.
- [18] G. New, "Pulse evolution in mode-locked quasi-continuous lasers," *IEEE J. Quantum Electron.*, vol. 10, no. 2, pp. 115–124, Feb. 1974.
- [19] J. L. A. Dubbeldam, J. A. Leegwater, and D. Lenstra, "Theory of mode-locked semiconductor lasers with finite absorber relaxation times," *Appl. Phys. Lett.*, vol. 70, no. 15, pp. 1938–1940, 1997.
- [20] R. Paschotta and U. Keller, "Passive mode-locking with slow saturable absorbers," *Appl. Phys. B*, vol. 73, no. 7, pp. 653–662, 2001.

Mattia Rossetti received the Laurea degree in physical engineering in 2007 from the Politecnico di Torino, Turin, Italy, where he is currently working toward the Ph.D. degree in electronic and communication engineering.

He is currently with the Dipartimento di Elettronica, Politecnico di Torino. His current research interests include the simulation of quantum-dot-based optoelectronic devices.

Paolo Bardella received the Laurea degree in electronic engineering and the Ph.D. degree in electronic and communication engineering from the Politecnico di Torino, Turin, Italy, in 2001 and 2006, respectively.

He is currently a Post-Doctoral Fellow with the Dipartimento di Elettronica, Politecnico di Torino, where he works on the simulation of multisection semiconductor lasers in mode-locking and self-pulsating regime. His current research interests include modeling and design of multisection quantum-dot semiconductor lasers and super-luminescent diodes.

Ivo Montrosset (M'92) was born in Aosta, Italy, in 1946. He received the Laurea degree in electronic engineering from the Politecnico di Torino, Turin, Italy, in 1971.

He is currently with the Dipartimento di Elettronica, Politecnico di Torino. From 1972 to 1986, he was with the Politecnico di Torino. In 1986, he was appointed Full Professor at the Università di Genova, Genova, Italy. Since 1990, he has been Full Professor of optoelectronics at Politecnico di Torino. His main research interests include guided-wave optics, solid-state and semiconductor lasers, and other related topics.

Prof. Montrosset is a member of the IEEE Photonics Society.